Temperature-responsive tungsten doped vanadium dioxide thin film starves bacteria to death

Jinhua Li [1,2,4,†], Wei Liu [3,†], Xianlong Zhang [3,*], Paul K. Chu [2,*], Kenneth M.C. Cheung [1], Kelvin W.K. Yeung [1,4,*]

[1] Department of Orthopaedics and Traumatology, Li Ka Shing Faculty of Medicine, The University of Hong Kong, Pokfulam, Hong Kong 999077, China
[2] Department of Physics and Department of Materials Science and Engineering, City University of Hong Kong, Tat Chee Avenue, Kowloon, Hong Kong 999077, China
[3] Department of Orthopaedics, Shanghai Jiao Tong University Affiliated Sixth People's Hospital, Shanghai Jiao Tong University, Shanghai 200233, China
[4] Shenzhen Key Laboratory for Innovative Technology in Orthopaedic Trauma, The University of Hong Kong-Shenzhen Hospital, Shenzhen 518053, China

The colonization of microorganisms on material surfaces, or namely biofouling, is a challenging matter in both the medical and marine industries. With the inspiration of the metabolism cascade of microorganisms, this study develops a new antifouling material surface that enables the drainage of extracellular electrons from the electron transfer chain in microbial metabolism, thereby interrupting the energy metabolism and subsequent microbial viability. This thought has been realized by tungsten-doped vanadium dioxide (VO_2) thin film using customized magnetron-sputtering deposition. The aim of tungsten doping is to tune the semiconductor-to-metal phase change of the VO_2 thin film and then endow the temperature-responsive electrical conductivity (band structure). While contacting with microorganisms, the electrically conductive VO_2 can disrupt the membrane respiration function of bacteria. This antifouling phenomenon can be explained by a three-step mechanism. The initial step is the microbial adhesion onto the metallic VO_2 film to form the direct microbe–VO_2 physical contact, which leads to the destructive extraction of electrons from the transmembrane protein complex of the respiratory chain (a discharge process); this induces oxidative stress and energy starvation and, eventually, interrupts the microbial membrane function. Finally, the microbial membrane integrity is destroyed, which leads to intracellular matter leakage (electrocution). This study demonstrates that the temperature-dependent VO_2 electrical conductivity or band structure serves as a key factor to modulate the antimicrobial capability of tungsten-doped VO_2 thin film. It is believed that the current findings can provide a new insight for the development of new antifouling surfaces.

Introduction

Biofilms produced by bacteria, which are a matrix of extracellular polymeric substances, always contaminate infrastructure devices and systems (i.e., biofouling), which produce huge social and economic burdens [1–3]. For instance, medical biofouling initiates biofilm accumulation on biomedical devices such as orthopedic and dental implants, catheters, biosensors, and surgical instruments, in which biofilms are the common cause of persistent infections [4–6]. Once mature biofilms are developed, they frequently challenge the efficacy of antibacterial treatments, specifically among antibiotic-resistant bacteria [7–9]. Although

* Corresponding authors at: Department of Orthopaedics and Traumatology, Li Ka Shing Faculty of Medicine, The University of Hong Kong, Pokfulam, Hong Kong 999077, China (K.W.K. Yeung).
E-mail addresses: Zhang, X. (dr_zhangxianlong@163.com), Chu, P.K. (paul.chu@cityu.edu.hk), Yeung, K.W.K. (wkkyeung@hku.hk).
† Jinhua Li and Wei Liu contributed equally to this work.

https://doi.org/10.1016/j.mattod.2018.04.005

applying antibiotics can effectively prevent or treat bacterial infections, antibiotic resistance has become a serious issue with the development of multidrug-resistant pathogens [10,11]. The bacterial contamination of various surfaces remains a worldwide research challenge [12,13]. Consequently, researchers are constantly attempting to design new antifouling/antimicrobial coatings to prevent bacterial attachment and subsequent biofilm formation.

Bacteria perform respiration to produce energy to conduct vital movements [14]. Bacterial respiration requires extracellular electron transportation, in which electrons are donated by nicotinamide adenine dinucleotide (reduced form of NADH). Then, the electrons are transferred to a terminal acceptor through a range of redox cofactors located in the bacterial membrane [15–20]. Inspired by this bioenergetic process, we assume that the interruption of extracellular electron transportation by engineering the specific nanoparticles in contact with bacteria can disrupt membrane respiration and cause bacteria inactivation. The equivalence of bandgap and Fermi energy levels plays a critical role in allowing electron transportation between the semiconductor and bystander. If a conductive circuit between the bacterium and semiconductor surface can be established, electrons generated within the bacterium will continuously drain out via electron transportation and then interrupt bacterial viability.

Vanadium dioxide (VO_2) is a thermochromic material that undergoes a reversible semiconductor–metal transition from a high-temperature rutile phase ($P4_2/mnm$, R) to a low-temperature monoclinic phase ($P2_1/c$, M1) at a critical temperature (Tc) of ~340 K under external temperature stimuli or near-infrared irradiation [21–25]. Concomitant with the phase transition are discontinuous jumps in electrical conductivity, optical transmittance, magnetic susceptibility, specific heat, and the Seebeck coefficient [26,27]. To consider the significant features and advantages of VO_2, we propose to tune the thermochromic property of VO_2 by doping tungsten into its matrix to modulate the electrical conductive property, which can potentially interrupt the extracellular electron transportation of bacteria upon contacting with VO_2 thin film, and thus achieve a superior antifouling effect.

The aim of this study is to design a phase-change-tunable VO_2 antifouling coating that is triggered by the change in the temperature of the micro-environment. The VO_2 thin films were prepared using a customized magnetron-sputtering technique, and tungsten doping was applied simultaneously. The changes in the thermochromic and electrical properties of the VO_2 thin films after tungsten doping were systematically investigated. Then, the in vivo antimicrobial ability was analyzed using a rat subcutaneous infection model induced by methicillin-resistant *Staphylococcus aureus* (MRSA). To understand how the antimicrobial effect of this newly developed thin film occurs in an in vivo condition, additional in vitro experiments were performed to investigate the interactions between the bacteria and VO_2. Finally, a series of physical parameters were determined using ultraviolet photoemission spectroscopy (UPS), activation energy, and the Hall effect measurements to support the proposed antifouling mechanism.

Materials and methods

Sample preparation

Pure VO_2 and tungsten-doped VO_2 thin films were prepared by a magnetron-sputtering apparatus (Plasma Technology Ltd., MS400). Fused quartz glasses with the size of 10 × 10 × 0.5 mm were adopted as substrates. To obtain tungsten-doped VO_2 thin films, vanadium dioxide and tungsten trioxide ceramic targets were used. During the deposition process, the DC power of VO_2 target maintained at 80 W, while the RF power of WO_3 varied (5 W, 15 W, and 30 W). The thicknesses of the films were detected by an F20 thin-film analyzer (FILMSTRICS Corp.). All undoped and doped thin films had the same thickness of 50 nm implemented by regulation of the deposition time. Bare quartz glass functioned as the control group. For simplicity, undoped VO_2 thin-film sample is denoted as *VO_2*, while the doped samples with RF power = 5 W, 15 W, and 30 W are labeled as *VO–W1*, *VO–W2*, and *VO–W3*, respectively.

Sample characterization

A field-emission scanning electron microscope (SEM; HITACHI S-4800, Japan) was used to observe the surface morphology of samples *VO_2*, *VO–W1*, *VO–W2*, and *VO–W3*. X-ray diffractometer (XRD; Rigaku Ultima IV) was used to study the crystalline structure of films, fitted with Cu Kα radiation (λ = 1.541 Å) at a voltage of 40 kV and current of 40 mA. The XRD patterns were recorded in the range of 20°–80° (2θ) with a step size of 0.02° and scanning rate of 2°/min. For the X-ray diffraction test, the glancing incidence angle was fixed at 1°. Phase identification was performed with the help of the standard JCPDS database. The chemical composition and chemical state were studied by X-ray photoelectron spectroscopy (XPS; Thermo Scientific Escalab 250Xi, US) with Al K^{α} (1486.6 eV) illumination. Argon ion sputtering with an acceleration voltage of 2 kV for 30 s was performed prior to the XPS measurement to obtain a clean surface of each sample. Ultraviolet photoelectron spectroscopy (UPS) measurements were performed on all the samples at room temperature with the use of XPS testing system. Emission of He I with photon energy of 21.2 eV was used as a light source. The AFM image was collected using a Nanocute SII scanning probe microscopy operated in tapping mode under ambient conditions. Etched N-type Si nanoprobe tips with a spring constant of 40 N/m and resonance frequency of 200–400 kHz were adopted. Resistance versus temperature curves were conducted with a four-probe testing system (JANIS Research co., Model VPF-100) equipped with a temperature controller (Cryogenic Control System, Inc., Model 32/32B, USA) and a Keithley 2400 digital source meter. The schematic of this customized testing system and experimental details can be found in this Ref. [28]. The optical transmittance characteristics were monitored by the UV–visible–near-IR spectrophotometer (Hitachi U-3010) equipped with an attachment to control the temperature of the films. The precise temperature was measured using a PT100 temperature sensor in contact with the surface of films, and the temperature was controlled via the temperature controlling unit. The transmittance spectra were collected from 350 nm to 2600 nm, and the transmittance curve of the quartz glass was used as a baseline calibration for the transmittance measurements. Hysteresis loops were measured by

collecting the transmittance spectra of samples at the fixed wavelength of 2000 nm with a heating–cooling rate of 2.0 °C/min. The electron transport properties of the films were characterized by the Hall effect measurement system (Lakeshore, 7704A) at room temperature using a four-terminal van der Pauw configuration. To obtain the work function of the prepared thin films, a series of Kelvin Probe Force Microscopy (KPFM) measurements were performed using an atomic force microscope (Dimension ICON, Bruker co., USA), and the temperature of each sample was maintained at 37 °C (incubator temperature) using a heating stage.

In vivo antimicrobial test

Sample preparation: The samples *Control*, *VO_2*, *VO–W1*, *VO–W2*, and *VO–W3* in size of $10 \times 10 \times 0.5$ mm were used in the in vivo test. Rat implant-related subcutaneous infection model. The animal experiment was approved by the Animal Care and Experiment Committee of Sixth People's Hospital Affiliated to Shanghai Jiao Tong University. Fifty specific pathogen-free male Sprague–Dawley rats that were six months old and had an average weight of 450 g were randomly divided into five groups (*Control*, *VO_2*, *VO–W1*, *VO–W2*, and *VO–W3*). Methicillin-resistant Staphylococcus aureus (MRSA, ATCC43300, biofilm-positive) was used to develop the infection model. Prior to surgery, these rats were first anesthetized with 3% pentobarbital sodium via intraperitoneal injection; the hair on the anterior upper backs was shaved, and the skin area was sterilized with povidone iodine. Under sterile conditions, the skin was incised layer by layer and the samples were placed into the subcutaneous soft tissue immediately. Afterward, the suture of skin incisions was carefully completed. Then, 70 μl of prepared MRSA suspension ($\sim 10^7$ CFU/ml) in phosphate-buffered saline (PBS) was added into the subcutaneous surgical sites upon the implants.

Histological observation: The soft tissues around the implants of each group were collected and fixed in 10% buffered formalin at 4 °C for 3 d. Then, they were washed with fresh PBS, dehydrated in gradient alcohol solutions, and embedded in the paraffin. The samples were cut into sections using a sledge microtome (Leica, Hamburg, Germany). Finally, they were deparaffinized in the xylene solution, and Hematoxylin and Eosin (H&E) and May-Grünewald Giemsa staining was used to detect the histological changes on optical microscopy.

Microbiological evaluation: The subcutaneous implants in each group were aseptically taken out to quantitatively determine the numbers of bacteria in vivo. The implants were washed gently twice with fresh PBS to remove the planktonic bacteria. Afterward, they were immersed in 1 ml of PBS, sonicated for 10 min at 150 kHz (150 W, B3500S-MT, Branson Ultrasonics Co., Shanghai, China), and vortexed for 2 min (Vortex Genie 2, Scientific Industries, Bohemia, NY) to dislodge the adherent bacteria. Meanwhile, the soft tissues around the implants were acquired, weighed, and homogenized in sterile tubes containing 1 ml of PBS using a high-speed homogenizer (Jingxin Industrial Limited Company, Shanghai, China). The soft tissue homogenates were serially diluted in PBS, and 100 μl of diluent was evenly distributed on sheep blood agar (SBA). Finally, these plates were cultivated in an incubator statically at 37 °C overnight, and the numbers of bacterial colonies were counted using the spread plate method in line with the National Standard of China GB/T 4789.2 protocol.

In vivo toxicity evaluation

The major organs (heart, liver, kidney, and spleen) were harvested, fixed in 10% buffered formalin, processed routinely into paraffin, cut into sections, stained with H&E, and examined by optical microscopy.

In vitro antimicrobial assay

The biofilm-positive MRSA (ATCC43300) were used to evaluate the antimicrobial property of samples *Control*, *VO_2*, *VO–W1*, *VO–W2*, and *VO–W3*. The strain was first cultured in a fresh trypticase soy broth (TSB) medium at 37 °C overnight, and then according to the McFarland method, the inoculation concentration was adjusted to 10^6 CFU/ml in TSB. Each sample was positioned in a sterile 24-well plate, and 500 μl of prepared bacterial suspension was added into the wells containing samples. The 24-well plate was then kept in an incubator statically at 37 °C overnight.

Quantitative evaluation by SPM: After overnight culturing, the samples were taken out from the suspension with sterile tweezers and then gently dislodged with fresh PBS twice. Subsequently, each sample was placed in a sterile test tube containing 1 ml of fresh PBS and oscillated by an ultrasonic vibration instrument for 15 min and a vortex mixer for 1 min. The suspension with bacteria was acquired, and 100 μl of diluent bacterial suspension was evenly spread on SBA and cultured at 37 °C overnight. Then, the CFU number of viable bacteria on SBA was counted by SPM.

Microbial biofilm evaluation by confocal laser scanning microscopy (CLSM 510 meta; Zeiss, Germany). The surfaces of incubated specimens were gently washed with sterile PBS three times. Then, these samples were stained with 500 μl of mixed dye (LIVE/DEAD BacLight bacteria viability kits, Invitrogen) in a new 24-well plate, which remained in the dark for 20 min. Finally, the samples were lightly rinsed with fresh PBS and subsequently observed using CLSM. The viable microorganisms were stained in green, and the dead ones were stained in red.

Microbial biofilm evaluation by SEM: The incubated specimens were gently washed with fresh PBS three times, fixed with 2.5% glutaraldehyde overnight in a 4 °C freezer, and subsequently dehydrated in the following ethanol series (30, 50, 70, 80, 90,95 v/v%) for 10 min and in the absolute ethanol solution (twice for 10 min). Then the samples were desiccated , gold sprayed and examined using scanning electron microscopy (JEOL JSM-6310LV, Japan).

Physical measurements

The room-temperature electrical resistance and carrier density were acquired by the Hall effect measurements with a Lakeshore 7704A Hall System. The samples were tested with a size of 1×1 cm^2, and metal contacts were made with indium (In) dots using a four-point probe in the Van der Pauw configuration. UPS measurements were performed for all samples at room temperature in order to analyze electron states near Fermi level. Emission of He II with photon energy of 40.8 eV was used as a light source.

Statistical analysis

Statistically significant differences (P) between various groups were measured using a one-way analysis of variance and Tukey's multiple comparison tests on a GraphPad Prism 5 statistical software package. All the data were expressed as mean ± standard deviation (SD). A value of $P < 0.05$ was considered to be statistically significant and denoted as "*"; $P < 0.01$ was "**"; and $P < 0.001$ was "***".

Results

Sample characterization

The crystal structures of the as-prepared samples were characterized by X-ray diffraction (XRD). Fig. 1a shows XRD patterns of the as-prepared thin films with different W-doping fractions. For VO_2 thin film, only XRD peaks corresponding to the signal of the monoclinic VO_2 phase were observed, and all the positions of peaks were concordant with the standard reference data (JCPDS No. 72-0514), which indicated the exclusive formation of single-phase VO_2 polycrystalline films. For W-doped VO_2 thin films (sample *VO–W1*, *VO–W2*, and *VO–W3*), the peaks belonging to WO_3 could not be observed because W was doped into vanadium oxide as the solute donor, which indicated that W entered into the crystal lattice of the VO_2 matrix. In addition, most peaks of the doped VO_2 samples shifted slightly toward lower 2θ values. To clearly demonstrate the shift of (011) the main peak, a scan rate of 0.3° min^{-1} was applied to record the pattern of samples *VO_2*, *VO–W1*, and *VO–W2* in the 2θ range from 25° to 30°, as shown in the inset of Fig. 1a. Because the atom radius of W ($r = 1.41$ Å) is larger than that of V ($r = 1.35$ Å), when W atoms substitute V atoms in the VO_2 lattice, the adjacent interplanar distance $d(h\,k\,l)$ becomes larger and results in the shift of the peak toward a low 2 Theta angle [29]. The surface morphologies of prepared samples are presented

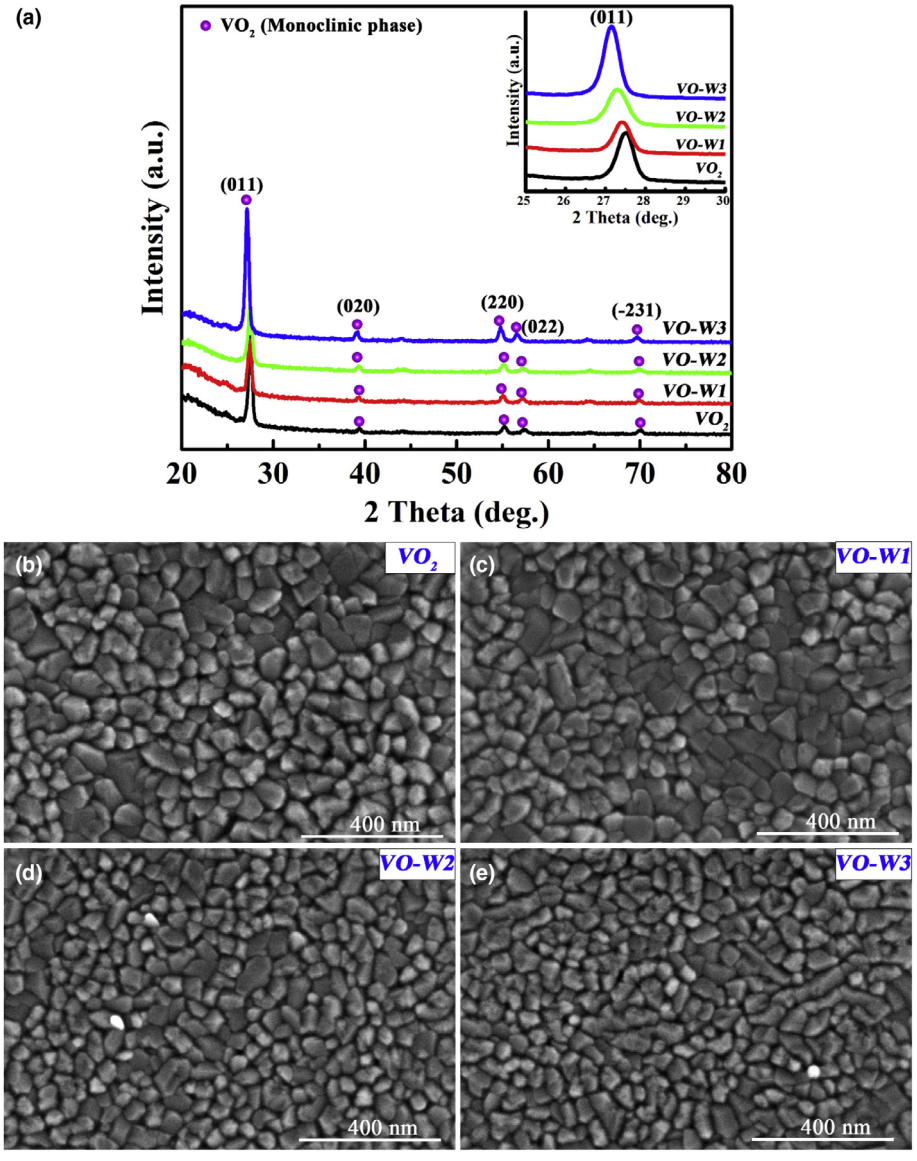

FIGURE 1

(a) XRD patterns and (b–e) SEM images of undoped and W-doped VO_2 thin films.

in Fig. 1b–e. Although doping with W makes the grains smaller to some extent, all the samples have similar morphology features. All crystalline grains have irregular shapes and sharp outlines. The RMS values obtained from the three-dimensional atomic force microscopy (AFM) images for *VO_2*, *VO–W1*, *VO–W2*, and *VO–W3* are 0.9, 4.9, 3.6, 3.1, and 4.2 nm, respectively (Fig. S1). The small RMS values indicate that the surface of the VO_2 thin film is extraordinarily smooth.

X-ray photoelectron spectroscopy (XPS) was also adopted to elucidate the valence state and content information. For pure VO_2 thin films (Fig. 2a), the binding energies of 515.6 eV and 523.0 eV correspond to the V $2p_{3/2}$ and V $2p_{1/2}$ core levels, respectively, of tetravalent vanadium (V^{4+}) [30]. The XPS result indicates that the prepared VO_2 thin film is pure without other valances, which is in accordance with the XRD results. The binding energy of 530.0 eV is the O 1s core level. Moreover, three W-doped VO_2 thin films also have the same binding energy of V and O elements (Fig. S2), which indicates that doping does not change the valance of V. For W-doped VO_2 thin films (Fig. 2b–d), the binding energies of 35.7 ± 0.1 eV and 37.8 ± 0.1 eV correspond to the W $4f_{7/2}$ and W $4f_{5/2}$ core levels [31,32], respectively. This implies that the valence of tungsten ion in the W-doped VO_2 thin film is +6. Moreover, the relative intensity of W $4f_{7/2}$ and W $4f_{5/2}$ core levels increases from sample *VO–W1* to *VO–W3*, which is ascribed to the increase in the W-doping concentration. The binding energy of 40.0 eV is the V 3p core level of tetravalent vanadium (V^{4+}) (Fig. 2b–d) [33]. The XPS compositional results also indicate the phase purity of the W-doped VO_2 sample. The atom percentage of elements is shown in Table S1. The doping atom percentages of samples *VO–W1*, *VO–W2*, and *VO–W3* are 0.26, 0.83, and 1.89 at.%, respectively.

The electrical resistance versus temperature curves were plotted to explore the electrical transport characteristics of undoped and doped VO_2 thin films under different temperatures. As shown in Fig. 3a, the resistance of all the samples presents a huge contrast between the low-temperature semiconductor phase and the high-temperature metallic phase. The difference is especially remarkable across the transition region. The resistance ratio, as shown in Table S2, is defined as the ratio of the resistance at 40 °C below the respective transition temperature *Tc* ($R_{(Tc-40)}$) and the resistance at 40 °C above the *Tc* ($R_{(Tc+40)}$), which changes from 385 to 84 from sample *VO_2* to *VO–W2*. The transition temperature (T_c) is defined as the center temperature of the thermochromic hysteresis. The doping content of the W element plays a great role in the transition temperature of VO_2. For pure VO_2 thin film, the transition temperature is 61 °C (334 K). The transition temperature of VO_2 thin film is lower than that of bulk crystal (T_c = 340 K); this is attributed to the internal stress produced by the ion bombardment effect during the film growth process. After doping 0.26, 0.83, and 1.89 at.% of W element, the T_c was 53 °C, 36 °C, and 8 °C, respectively. Obviously, the T_c values for pure VO_2 thin film and sample *VO–W1* are above the incubator temperature (37 °C = 310 K) of bacteria and cells. The T_c value for *VO–W2* approaches to the incubator temperature,

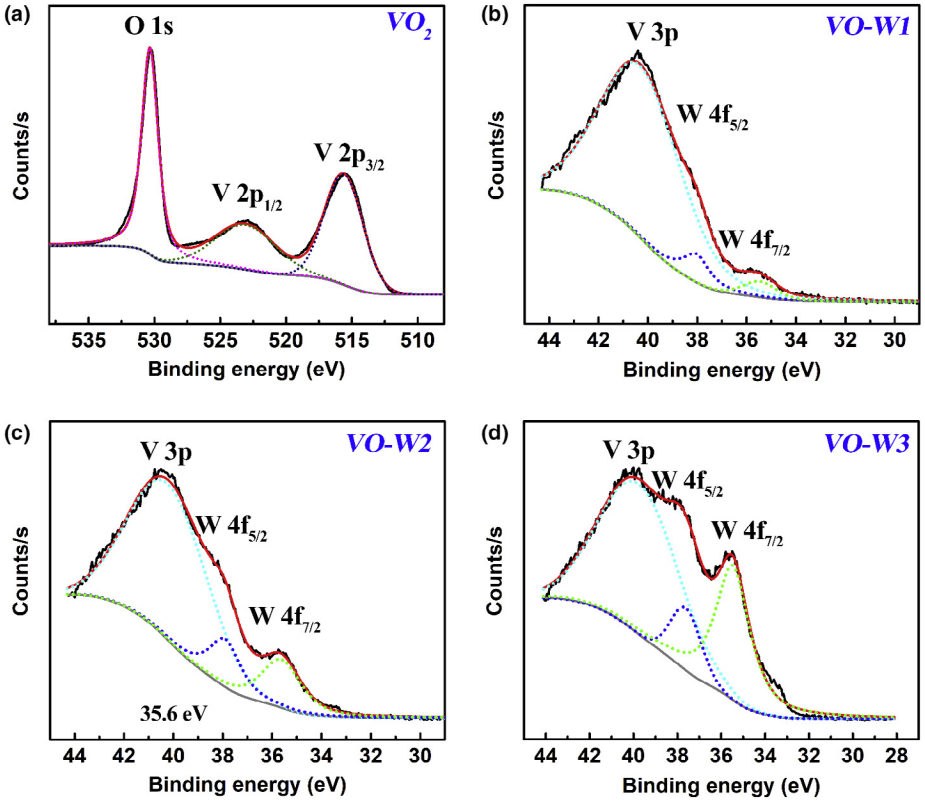

FIGURE 2

(a) XPS analysis result showing the V 2p and O 1s XPS spectrum obtained from the surface of pure VO_2 thin film. XPS analysis result showing the V 3p and W 4f XPS spectrum obtained from the surface of samples (b) *VO–W1*, (c) *VO–W2,* and (d) *VO–W3*. Notes: black solid curves, raw data; red solid curves, fitted data; gray solid curves, Shirley background; dashed curves, fitted peaks.

while the T_c value for *VO–W3* is below that, as shown in Fig. 3b. The results are apparent that both pure VO_2 thin film and *VO–W1* are in semiconducting state at the incubating temperature, while *VO–W3* sample is in metallic state. It is believed that the intermediate *VO–W2* appears in a mixed state between semiconducting and metallic phase. The depression in phase transition upon W doping arises from destabilization of the V–V dimers in the M1 phase probed by local X-ray absorption fine structure spectroscopy [34]. Tungsten is found to be displacively doped within VO_2 as W^{6+} and forms two distinctive pairs with valences of V^{3+}–W^{6+} and V^{3+}–V^{4+} to maintain the charge neutrality of the lattice. The destabilization of the M1 phase thus reduces the potential energy barrier for transformation to the rutile structure. Additionally, the ionization of the tungsten dopant to W^{6+} adds two electrons to the band structure of VO_2, which further increases the carrier density and coaxes the system toward transformation to the metallic state [26].

Transmittance is another indicator of the variation of thermochromic performance after doping treatment. The transmittance of thin films measured at relatively low temperatures (30 °C, solid curves) and high temperatures (90 °C, dashed curves) are exhibited in Fig. 3c. Pure VO_2 and three W-doped VO_2 thin films (especially *VO–W1* and *VO–W2*) exhibit an obvious transmittance contrast between the low-temperature semiconductor phase and high-temperature metallic phase, especially in the near-infrared region, which is ascribed to the thermochromic nature of VO_2. The plasma frequency (ω_p) of the metallic state VO_2 is reported to be 1.0 eV (~1240 nm) or 1.6 eV (~775 nm); thus, the rutile phase has a lower transmittance in the IR region because the incident light at a frequency below the plasma frequency leads to motion in the charge carriers, which screens out the incident field, in other words, reflects the incident waves. The increase in W-doping content results in the shrink of the transmittance contrast between the two phases. This difference is mainly caused by a relatively low testing temperature (30 °C) because all the samples have completely transformed into the metallic phase under a relatively high testing temperature (90 °C). For sample *VO–W2*, the transmittance in both phases is low and the contrast is minimum because the transition temperature of *VO–W2* is 8 °C, which is much lower than the test temperature (30 °C); thus, the metallic phase fails to completely transform into the semiconductor phase. On the contrary, for sample *VO–W1*, almost all the grains are in the semiconductor phase because its transition temperature is much higher than the test temperature (30 °C), while for sample *VO–W2*, whose transition temperature is near the test temperature, part of the grains is in the semiconductor. The optical transmittance of the sputtered films at the fixed wavelength of 2000 nm was studied as a function of temperature from 35 °C to 95 °C. The thermal hysteresis loops are clearly shown in Fig. 3d. The loops in the transmittance spectra are similar to those in the resistance curves and confirm the depression of transition temperature after W-doping treatment.

In vivo antifouling performance

H&E and Giemsa staining were performed for histological evaluation to observe morphology change and microbe amounts in

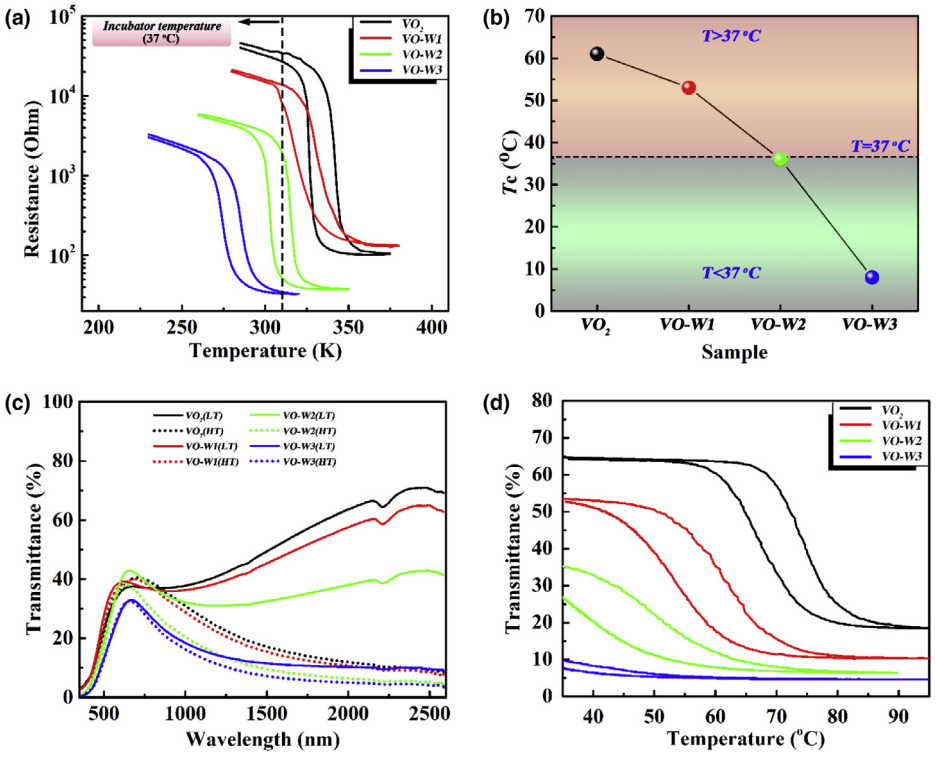

FIGURE 3

(a) Resistance vs temperature curves and (b) transition temperature of prepared samples; the incubator temperature of 37 °C is pointed out as a reference. (c) Optical transmittance spectra of samples *VO_2*, *VO–W1*, *VO–W2*, and *VO–W3* measured at low temperature (LT = 30 °C, solid curves) and high temperature (HT = 90 °C, dashed curves). (d) Thermal hysteresis loops of the optical transmittance of undoped and W-doped thin films at a fixed wavelength of 2000 nm.

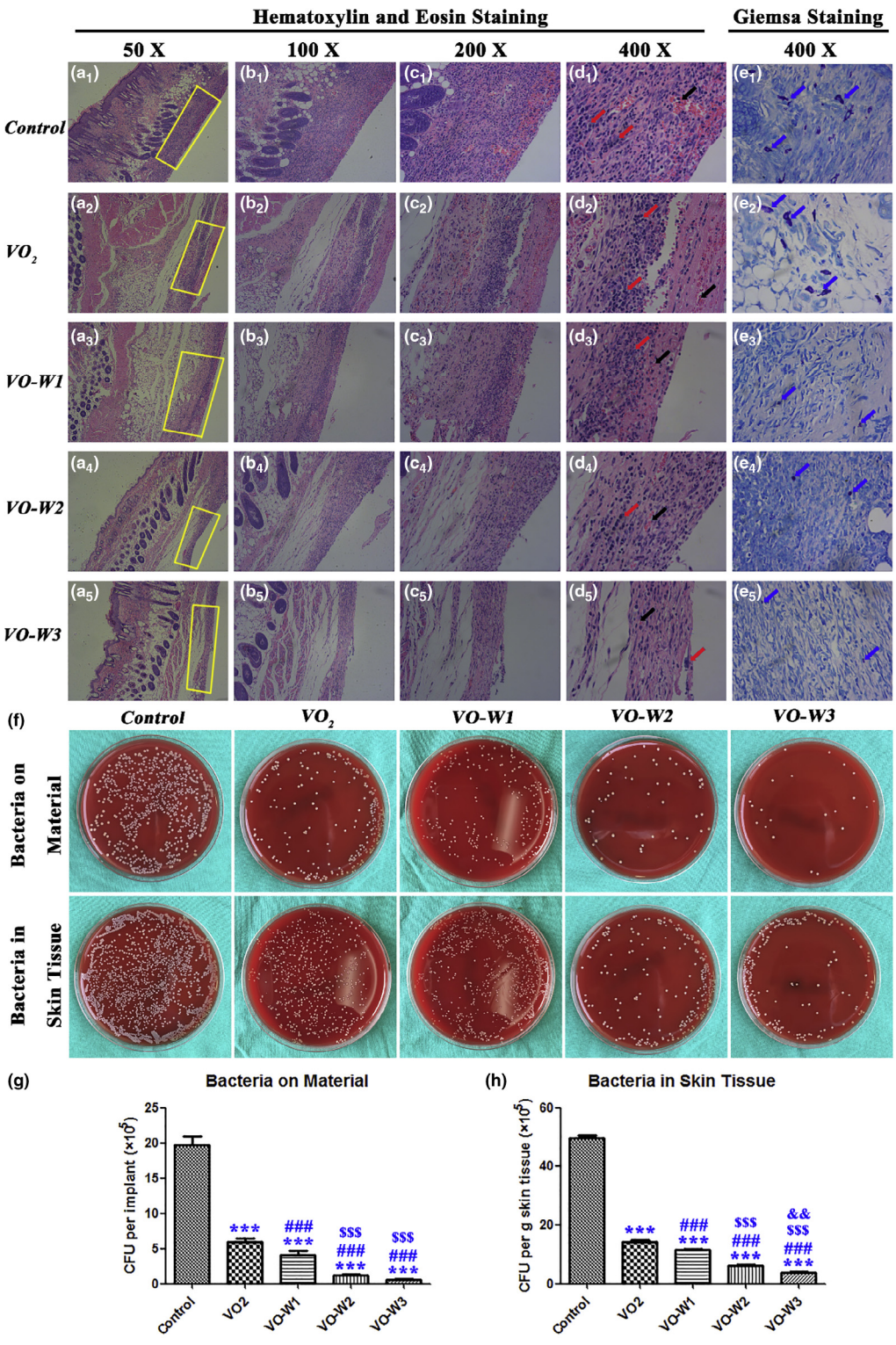

FIGURE 4

(a–e) Representative photomicrographs of histological slices perpendicular to the samples, stained with H&E and Giemsa staining at 14 d after operation. Close-up micrographs (from left to right, ×50, ×100, ×200 and ×400): higher magnification of H&E-stained soft tissues at the implant–tissue interface of the labeled area in the former micrographs. Red arrows point the neutrophil infiltration. Black arrows indicate the macrophage phagocytosis. Rightmost column (×400): magnification of Giemsa-stained peri-implant soft tissues in various groups. Blue arrows manifest the microbe residues. *Control* group, VO_2 group: H&E-stained views (a_1–d_1, a_2–d_2) show serious feature of soft tissue infection, large numbers of neutrophil infiltration, and inflammatory exudation at the implant–soft tissue interface. Meanwhile, many microbes exist in the adjacent soft tissues (e_1 and e_2). *VO–W1* group: H&E images (a_3–d_3) represent less inflammatory response, neutrophil infiltration, and fewer microbial burdens in soft tissues surrounding the implant (e_3). *VO–W2* group, *VO–W3* group: H&E micrographs (a_4–d_4, a_5–d_5) reveal the mildest inflammatory reaction and the fewest neutrophils and microbes present in the soft tissues (e_4, e_5). (f) Representative photographs of bacteria colonies re-cultivated from the implants and peri-implant soft tissues, accompanied by the corresponding quantification of live bacteria (g) on materials and (h) in soft tissues. *Note:* $^{***}P < 0.001$ vs *Control*; $^{\#\#\#}P < 0.001$ vs VO_2; $^{\$\$\$}P < 0.001$ vs *VO–W1*; $^{\&\&}P < 0.01$ vs *VO–W2*.

peri-implant soft tissue. For the control (Fig. 4a1–d1), the typical representation of soft tissue infection was observed at the interface between quartz glass and circumambient soft tissue, and there existed apparent acute inflammation, tissue necrosis, and extensive neutrophil infiltration into the soft tissue. In the meantime, the corresponding Giemsa staining slice confirmed the presence of large numbers of microbes at the implant–tissue interface (Fig. 4e1). To some extent, those situations were improved for sample *VO_2* (Fig. 4a2–e2). With a sharp contrast, according to the H&E and Giemsa staining slices, sample *VO–W1* (Fig. 4a3–e3) and *VO–W2* (Fig. 4a4–e4) showed more moderate inflammatory response, lower neutrophil infiltration, and less microbe residue. Sample *VO–W3* displayed the mildest inflammatory reaction and lowest amount of microbe residue at the implant–soft tissue interface (Fig. 4a5–e5). As a result, *the* in vivo anti-infection effect showed a strong dependence on the conductivity of the underlying substrate (i.e., undoped and doped VO_2 films).

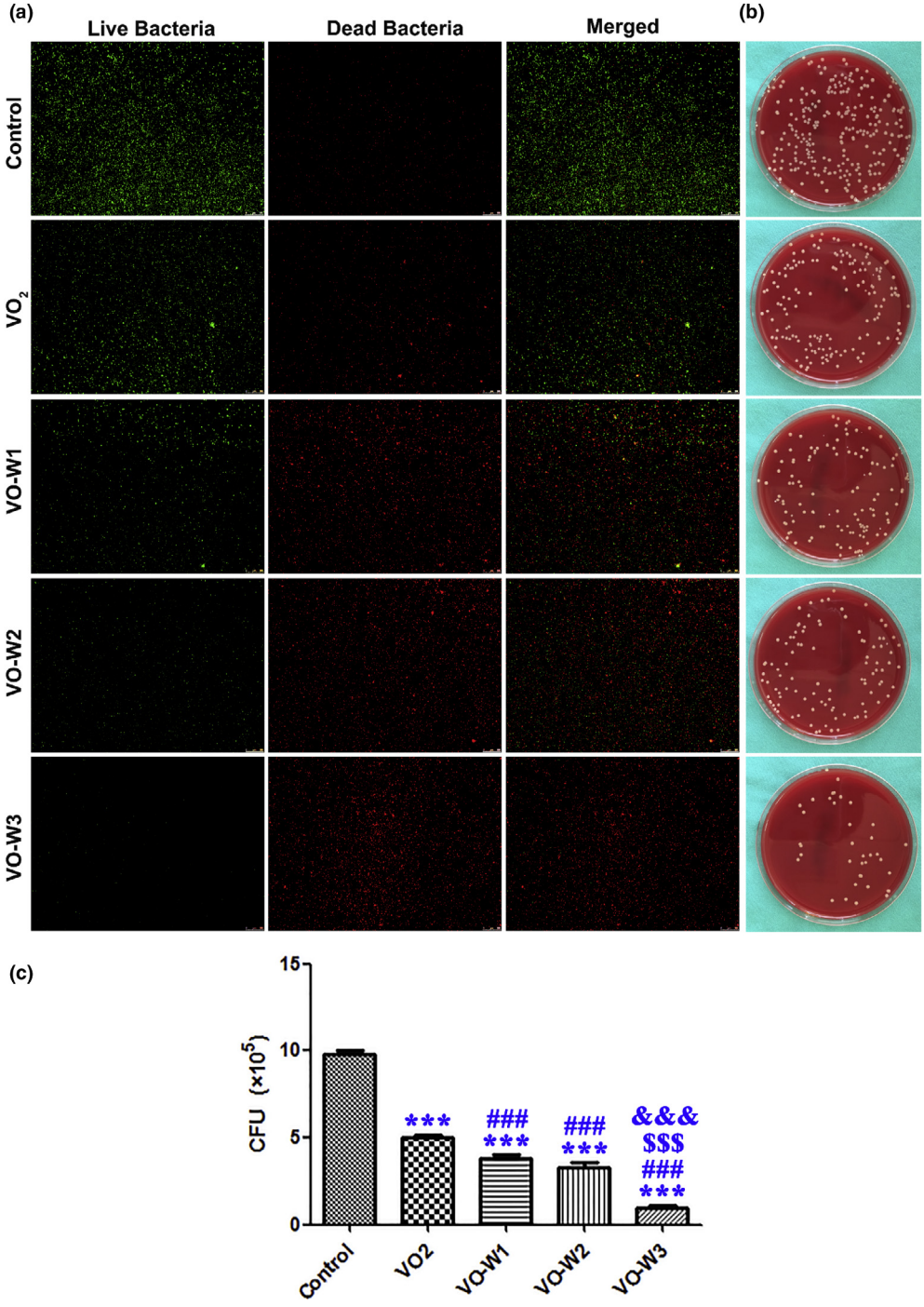

FIGURE 5

(a) Live/dead fluorescence staining results of the MRSA bacteria on the samples *Control*, *VO_2*, *VO–W1*, *VO–W2,* and *VO–W3*. (b) Representative photographs of bacteria colonies re-cultivated from the surfaces of various samples. (c) The corresponding quantification results of live MRSA bacteria. *Note:* $^{***}P < 0.001$ vs *Control*; $^{\#\#\#}P < 0.001$ vs *VO_2*; $^{\$\$\$}P < 0.001$ vs *VO–W1*; $^{\&\&\&}P < 0.001$ vs *VO–W2*.

We then used the spread plate method to quantify the microbial burden from the quartz glass and peri-implant skin tissue. Representative photographs of microbial colonies are given in Fig. 4f. According to the corresponding counting results of the colony forming units (CFU) per implant (Fig. 4g) and CFU per g skin tissue around the implant (Fig. 4h), the average number of CFU per implant demonstrated the following trend ($\times 10^5$): *Control* (19.69 ± 1.27) > *VO_2* (5.90 ± 0.52) > *VO–W1* (4.05 ± 0.63) > *VO–W2* (1.21 ± 0.15) > *VO–W3* (0.57 ± 0.15), and there was an apparent statistical difference among the groups ($P < 0.001$). The mean number of CFU per g peri-implant skin tissue showed a similar trend ($\times 10^5$): *Control* (49.63 ± 0.84) > *VO_2* (14.41 ± 0.44) > *VO–W1* (11.59 ± 0.40) > *VO–W2* (6.16 ± 0.26) > *VO–W3* (3.85 ± 0.24), and there was a significant difference among the groups ($P < 0.01$). Interestingly, when we put them together for comparison, as shown in Fig. S3, the number of CFU in skin tissue was obviously larger than the corresponding number of CFU on material with significant statistical difference ($P < 0.001$), thus indicating that the antimicrobial incident mainly occurred on the surface of VO_2 and W-doped VO_2 films. This has suggested that the conductivity of the film materials plays an important role in the antimicrobial behavior; in other words, high conductivity contributes to diverting electrons from bacteria.

In vitro antimicrobial performance

To further reveal the in vivo antimicrobial behaviors of the VO_2 and W-doped VO_2 samples, we performed the in vitro antimicrobial test. As seen in Fig. 5a, the viability of MRSA was visualized by live/dead staining after 24 h of culture on various samples, and the red fluorescent intensity increased clearly in the order of *Control*, *VO_2*, *VO–W1*, *VO–W2*, and *VO–W3*, thus confirming the significant loss of MRSA viability upon direct physical contact. SEM observation was also used to examine the morphology of MRSA on various samples. Large numbers of microbes were observed on the control sample with continuous biofilms (Fig. S4a). After VO_2 deposition, this situation was ameliorated to some degree (Fig. 5b). By W doping, the number of microbes sharply decreased in *VO–W1* (Fig. S4c), and this antimicrobial effect became increasingly powerful for *VO–W2* (Fig. S4d) and *VO–W3* (Fig. S4e). Meanwhile, significant microbial lysis was also observed on the W-doped VO_2 films. Therefore, the SEM observations were in accordance with the live–dead staining results, thus confirming the conductivity-dependent antimicrobial activity of the VO_2 and W-doped VO_2 films.

The spread plate method was used to quantify the number of MRSA on materials. Representative photographs of microbial colonies are shown in Fig. 5b. The mean CFU/ml values of *Control*, *VO_2*, *VO–W1*, *VO–W2*, and *VO–W3* were ($\times 10^5$) as

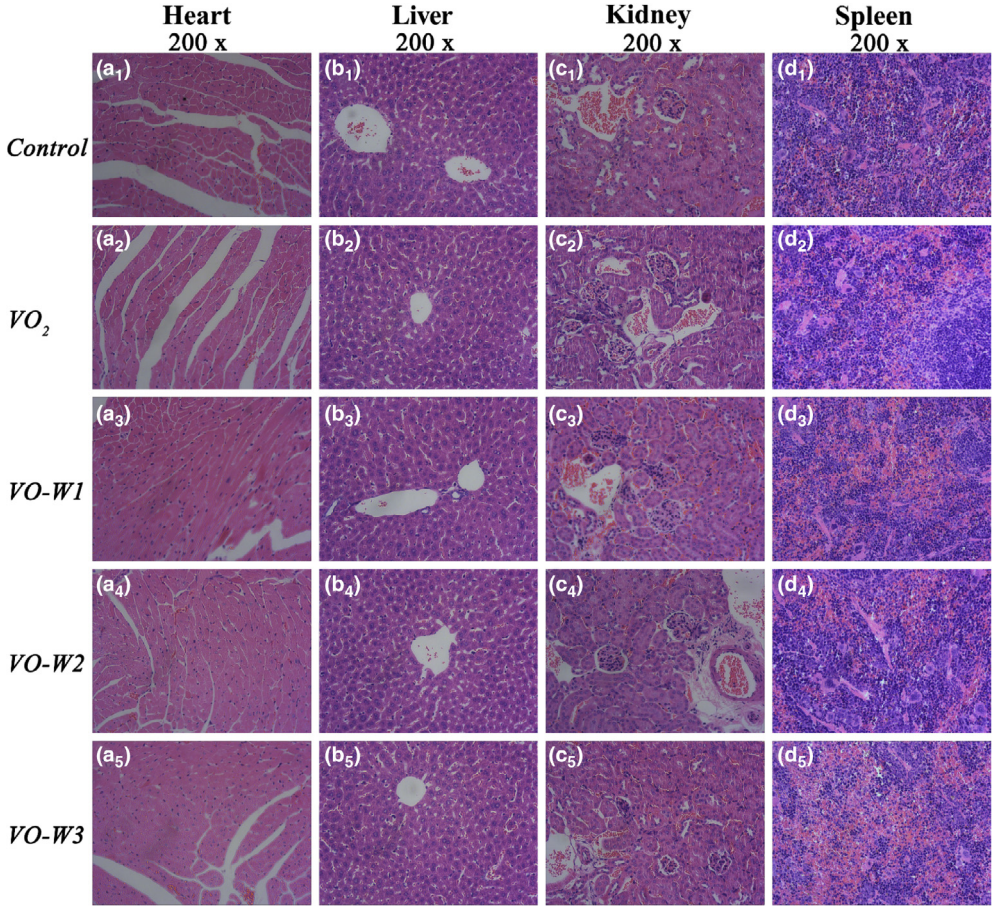

FIGURE 6

Histological sections of important organs including the heart, liver, kidney, and spleen after the implantation of samples *Control*, *VO_2*, *VO–W1*, *VO–W2*, and *VO–W3*, stained with H&E.

follows: 9.78 ± 0.23, 4.99 ± 0.17, 3.77 ± 0.23, 3.25 ± 0.31, and 0.98 ± 0.11 (Fig. 5c). Compared with the control group, VO_2 exhibited good anti-biofilm properties ($P < 0.001$), and remarkably, W doping further enhanced the anti-biofouling activity ($P < 0.001$). Meanwhile, the promoting effect was conductivity-dependent. Sample *VO–W3* can exert a more powerful antimicrobial effect than samples *VO–W1* and *VO–W2* ($P < 0.001$). Overall, it was found that tuning the thermochromism of VO_2 films by W doping can effectively modulate the film conductivity, and thus determine the antimicrobial behavior. In addition, the corresponding histological changes of main organs, including the heart, liver, kidney, and spleen, were examined by H&E staining. As seen in Fig. 6, no apparent signals of organ damage can be observed from all the groups. Meanwhile, the proliferation results of rat bone mesenchymal stem cells (rBMSCs) in Fig. S5 also show the samples had no significant cytotoxicity on rBMSCs. In accordance with the endosymbiotic theory (symbiogenesis), eukaryotic mitochondrion is an analog of prokaryote bacteria. However, the electron transport chain of mammalian cell for respiration is located in the intracellular mitochondria. Therefore, its electron transport chain is not interrupted, and the cell can survive on the surfaces.

Physical parameters

To further unravel the mechanism of the enhanced anti-biofouling capability subject to phase-change temperature of VO_2 films, we then investigated the influence of W doping on the band structure and electrical properties of VO_2 films. For semiconductor-phase VO_2, the bandgap between the top of the filled a_{1g} band (E_v) and the bottom of the empty e_g^{π} band (E_c) is produced by the splitting of V^{4+} 3*d* states. Intrinsic VO_2 thin film is *n* type [35]. In thermal equilibrium, the electron density in the conduction band $P(N) = 2[2\pi m_{p(n)}kT/h^2]^{1/2}\exp(-\triangle E_a/kT)$ is derived from the Fermi–Dirac distribution function, where $m_{p(n)}$ is the electron effective, k is the Boltzmann constant, and h is the Planck constant. The activation energy is defined as $\triangle E_a = E_C - E_F$. The temperature scanning in the resistance measurements allows us to acquire the activation energy in the semiconductor phase. Based on the Arrhenius' law $R = R_0\exp(-E_a/k_BT)$, the activation energy values are obtained by fitting the resistance (Fig. 7a). For the undoped VO_2 thin film, the calculated activation energy in the semiconductor phase is 0.29 eV (Fig. 7b). After W doping, the activation energy ranged from 0.18 eV (*VO–W1*) to 0.14 eV (*VO–W3*). The *VO–W2* (0.17 eV) and *VO–W3* had relatively lower activation energy and thus

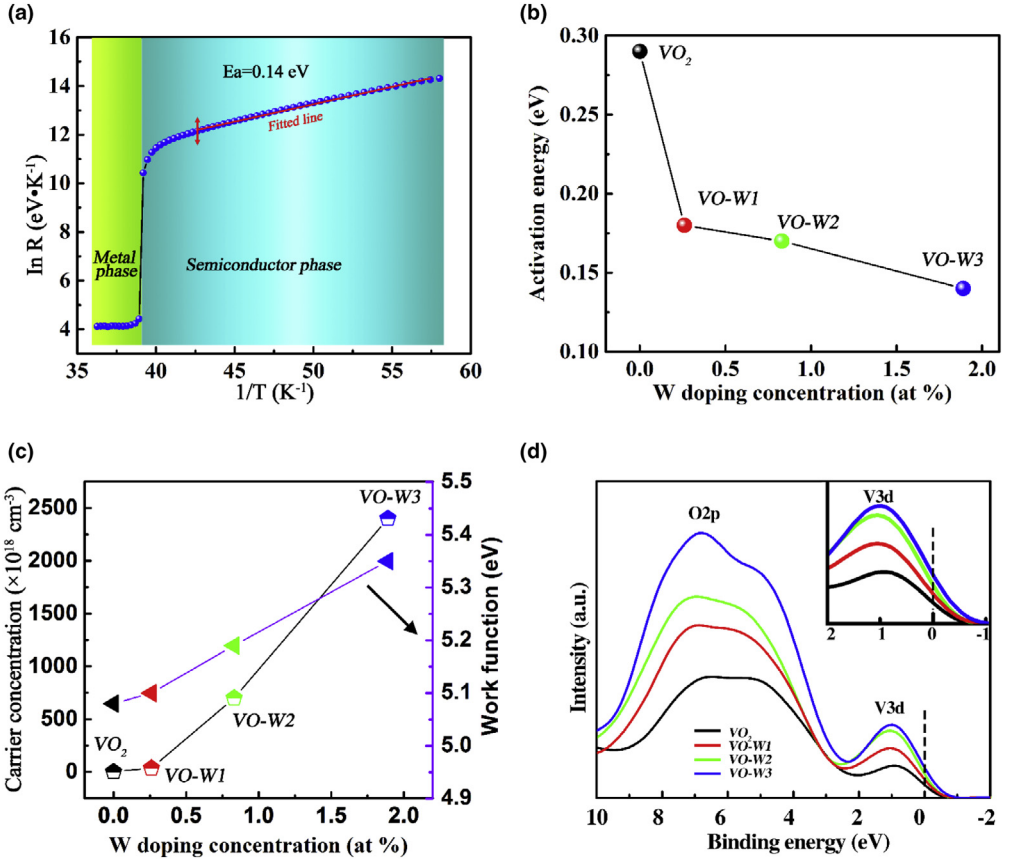

FIGURE 7

(a) The ln *R*~1/*T* curve of sample *VO–W3*; the activation energy in the semiconductor phase is determined by linearly fitting the curve. (b) Activation energies dependent on W-doping concentration. (c) The plot of carrier concentration versus W-doping concentration measured at room temperature by the Hall effect device and the plot of average work function versus W-doping concentration measured at 37 °C by Kelvin Probe Force Microscopy. (d) UPS spectra of samples VO_2, *VO–W1*, *VO–W2*, and *VO–W3*.

overall higher conductivity, which may be ascribed to donate electrons from d shells upon doping with tungsten.

To develop a further understanding of the electrical properties of these films, carrier concentrations were measured at room temperature using the Hall effect device, while the work function values were estimated by Kelvin Probe Force Microscopy at 37 °C. For pure VO_2 thin film and W-doped films, the electrons are the major contributors, as indicated by the sign of the Hall voltage. As shown in Fig. 7c, the carrier densities of samples *VO_2*, *VO–W1*, *VO–W2*, and *VO–W3* at room temperature were 2.5×10^{18}, 3.6×10^{19}, 7.0×10^{20}, and 2.4×10^{21}, respectively. These results are consistent with that of resistance value. Moreover, the increase in W-doping concentration may lead to the increment of work function slightly. For instance, the value of pure VO_2 thin film is 5.08 eV only. When 1.89 at.% W is doped on the film (sample *VO–W3*), the value has increased by 0.25 eV. The influence of W doping on the work function is similar to that of temperature rise. For example, Ko et al. [36] estimated that the work function of VO_2 is ~5.15 eV in the semiconductor phase. When it enters to the semiconductor–metal transition phase, the value increases by ~0.15 eV measured by KPFM. Martens et al. [37] also found that the work function of VO_2 evolves from 5.2 eV (room temperature) to 5.3 eV (100 °C), assessed by electrical characterization of VO_2-metal contact resistivity. However, a couple of previous studies presented the dichotomized results on the exact value and temperature dependence of the work function of VO_2. For instance, Sohn et al. [38] demonstrated that the work function drops from 4.88 eV to 4.70 eV when the semiconductor–metal transition phase is obtained. Similarly, Zhou et al. [39] suggested that work function of VO_2 decreases by ~0.2 eV when it goes through semiconductor–metal transition by the measurement of the electrical properties of GaN/VO_2 p–n heterojunctions. These discrepancies in the literatures may attribute to the microstructure, strain state [40], and surface stoichiometry of VO_2 when exposed to air/humidity [36] or in contact with other materials and the limitation of measuring machine (e.g., resolution limit). To confirm the aforementioned hypothesis, UPS measurement was carried out. The UPS spectra recorded from various films (Fig. 7d) represent successively increasing intensity near the Fermi level. For the samples of VO_2 and *VO–W1* in the semiconductor phase at room temperature and incubating temperature (37 °C), the UPS intensity, resembling approximately the density of occupied initial states, does not disappear near the Fermi level, presumably due to a strong V 3d band tailing into the bandgap, which is induced by the defects in the polycrystalline films. When the sample of *VO–W3* is fully in the metallic phase at either room temperature or 37 °C, the intensity in the range of the V 3d band does not disappear and remains higher than the intensity at the Fermi level. As a result, in the semiconducting state, fewer electrons occupy the Fermi level, and the occupancy increases as a function of W concentration. The occupancy in the metallic state is higher than that in the semiconducting state near the Fermi level [41]. Therefore, the change in the band structure of samples *VO_2*, *VO–W1*, *VO–W2*, and *VO–W3* agrees well with the development of the aforementioned electrical properties.

Discussion

The temperature of microbiological incubators is usually set at 37 °C, which mimics human body temperature. During surgery, medical devices such as implants, catheters, and surgical tools can undergo an ambient temperature change from room temperature to body temperature. The intrinsic thermochromic property can make VO_2 material undergo the reversible phase transition from a semiconducting state to a metallic state at the critical temperature (Tc) as an active response to ambient temperature stimuli or near-infrared irradiation, which is accompanied by discontinuous jumps in electrical conductivity. The extracellular electron transportation is a normal living movement for bacterial respiration. The adjustment of the phase-change/electrical property of VO_2 is important because it can potentially interfere with the extracellular electron transportation process of bacteria when contacting with them, thereby producing temperature-responsive VO_2 antifouling coating that can block bacteria colonization and prevent subsequent biofilm formation on medical devices.

First, we tuned the transition temperature of VO_2 thin films by altering the W-doping content to the desired range, namely, from 61 °C of *VO_2*, 53 °C of *VO–W1*, 36 °C of *VO–W2* to 8 °C of *VO–W3*, which led to the manipulation of the electrical properties of VO_2 thin films (Fig. 3, Table S2). This design reassures that (i) *VO_2* and *VO–W1* incubated at either room temperature or human body temperature are in a semiconducting state; (ii) *VO–W2* is certainly in a semiconducting state at room temperature, but a mixed state of semiconducting and metallic appears at human body temperature; and (iii) *VO–W3* is entirely in a metallic state, whether it is subject to room temperature or human body temperature. The resistance ratio between the two phases is slightly degraded with the increase in W-doping concentration, which is in accordance with previous reports [31,42]. The W-doping-induced resistivity decrease can be primarily attributed to several reasons. On the one hand, the substitution of V atoms with W in the VO_2 matrix leads to the tungsten oxidation state of 4+ and causes the valence band to be populated with tungsten *d* electrons. On the other hand, addition of tungsten may break V^{4+}–V^{4+} bonds and result in the formation of two new bonds: V^{3+}–W^{6+} and V^{3+}–V^{4+}. In this case, the resistivity decrease is due to the addition of released vanadium electrons from the d electronic shell [43]. Electrical conductivity (σ) describes how the ease of material (e.g., thin films) allows charges (e.g., electrons) to move or get through the material and it totally depends on the resistivity (ρ), as: $\sigma = 1/\rho$. Hence, the orders of electrical conductivity of the samples are: *VO–W3* > *VO–W2* > *VO–W1* > *VO_2*. The carrier concentration of the samples presents the same tendency as plotted in Fig. 7c. After that, we used a rat subcutaneous infection model to examine whether such a material design can influence the interactions between VO_2 coatings and microbial cells, and thus combat biofouling. As evidenced in Fig. 4, through tuning the semiconductor-to-metal transition of VO_2 thin films to alter electron concentration by W doping, the antifouling outcome can be very different among groups. With enhancing the film conductivity, the colonization of microorganisms on the coated implant or in the skin tissue adjacent to the implant can be sharply reduced, thus

displaying a mild inflammatory reaction and a low amount of microbial residue at the implant–skin tissue interface.

To determine the mechanism, we first cultured MRSA in vitro to investigate their response to pure and W-doped VO_2 thin films. As evidenced in Fig. 5, along with improving the film conductivity, the amounts of MRSA colonization on the coated samples were acutely decreased and exhibited favorable antibiofouling activity. These in vitro results agreed with and partially explained the in vivo outcomes. To further understand the underlying mechanism, we conducted a series of physical measurements on the band structures and electrical properties of the VO_2 and W-doped VO_2 thin films. As evidenced in Fig. 3, by virtue of W doping, the phase-change VO_2 thin films can be responsive to a range of environment temperatures, including body temperature, room temperature, and seawater temperature (30–8 °C [44]). Accompanied by this, the electrical properties of VO_2 thin films were modulated in a large range. The activation energies were significantly lowered from the *VO_2* group to *VO–W3* group (Fig. 7a and b). Accordingly, the carrier concentrations were apparently elevated from the *VO_2* group to *VO–W3* group, while the work function values were increased by 0.25 eV (Fig. 7c). Obviously, the change in the electrical conductivity also indicated the variation in the band structure of VO_2 thin films, which was further demonstrated by the results of UPS measurements (Fig. 7d). With reference to the values of activation energy and work function previously described, the band diagrams of doped and undoped VO_2 thin films can be interpreted.

In addition, the *VO–W3* group has exhibited superior antifouling ability than that of the *VO–W2* group. This observation can attribute to the higher electrical conductivity of *VO–W3* as compared with the sample of *VO–W2*. In fact, the *VO–W3* sample is already in a metallic state at either room temperature or human body temperature, whereas the *VO–W2* only appears in a mixed state of metallic and semiconducting at human body temperature. Hence, the antifouling abilities of the samples should be in the order of *VO–W3* > *VO–W2* > *VO–W1* > *VO_2*.

These results confirm a close relationship between the electrical conductivity (band structure) and antifouling activity of VO_2 thin films. Regarding the in vivo toxicity, the histological images of main organs (heart, liver, kidney, and spleen) shown in Fig. 6 demonstrate that all the implanted samples did not cause significant abnormalities or lesions, thus showing no apparent in vivo toxic side effects; moreover, as shown in Fig. S5, there was no significant cytotoxicity on rat bone mesenchymal stem cells. In fact, vanadium has been documented on the list of 40 essential micronutrients and are required in trace amounts for normal metabolism, proper growth, and development of mammals [45]. Vanadium deficiency causes growth inhibition, tooth, bone and cartilage growth impairment, generative function disorder, and lipids and carbohydrate metabolic pathways disturbance [45,46]. Some studies show that vanadium can enhance the mineralization of bones and teeth in laboratory animals [47] and can improve the integration of implant and soft tissue [48].

Our results demonstrated for the first time that the antimicrobial property of VO_2 correlates with its electrical conductivity or band structure. Extracellular electron transfer along the respiratory chain on the plasma membrane of microorganisms naturally proceeds through a sequence of the transmembrane protein complex, including complex I (consisting of the motifs for binding NADH, FMN and Fe-S cluster), complex II (succinate ubiquinone reductase), complex III (ubiquinone cytochrome c reductase), and complex IV (cytochrome c oxidase), as illustrated in Scheme 1a. Therefore, it is reasonable to consider that the leakage of electrons out of the electron transfer chain will jeopardize energy metabolism and microbial viability. The stronger antimicrobial activity of W-doped VO_2 films indicated that, after microbe–VO_2 physical contact and membrane perturbation, VO_2 exerted conductivity-dependent antifouling function. Due to the electrically conductive property, the VO_2 films of metallic state resulting from W doping could be able to "short-circuit" the microorganisms by acting as a conductive electron pump or electron trap that can destructively extract electrons from the electron transfer chain of microorganisms and release microbial energy into the extracellular environment. That is, not only can VO_2 films serve as conduits for extracellular electron transfer out of microbial plasma membrane but also the occurrence of the electron leakage shows strong dependence on the electrical conductivity or band structure of the thin films. Apparently, the aforementioned transmembrane protein complex is highly redox-active, as seen in Table S3. Thus, by tuning the electrical conductivity or band structure of VO_2 films, it is feasible to make extracellular electron transfer occur between the VO_2 films and redox-active bystanders [49,50].

The observations of live/dead staining (Fig. 5a) and SEM (Fig. S5) collectively demonstrate that the inactivation and death of MRSA should be largely attributed to the destruction of plasma membrane integrity. The sequence of transmembrane protein complex can shuttle electrons along the respiratory chain, normally to the terminal electron acceptor, dioxygen, and produce H_2O through complex IV. However, under external stimuli, such as exposure to metallic VO_2, the overproduction of reactive oxygen species (ROS) can be caused by electron leakage from the impeded electronic transport. For instance, electron leakage from the ubiquinone (CoQ) can induce the overproduction of $^{\cdot}O_2^-$ ($^{\cdot}CoQ^- + O_2 \rightarrow CoQ + {}^{\cdot}O_2^-$) [51] and other species in Table S4.

The mechanism of electrically conductive VO_2 thin films acting as antifouling coatings on a substrate to prevent biofilm formation is illustrated by a schematic diagram (Scheme 1). The elevated ROS production can cause oxidative damage to the plasma membrane, which may account for the observed destruction of MRSA membrane integrity [52]. Meanwhile, interruption of electron transport will also disturb the synthesis of adenosine triphosphate (ATP) [53]. At this stage, the observed antifouling process can be summarized in three steps. The first step is that microorganisms initially adhere or deposit onto the metallic VO_2 films to form direct microbe–VO_2 physical contact, followed by the destructive extraction of electrons from the transmembrane protein complex, a discharge process of respiratory chain, by the electrically conductive VO_2 films, which causes ROS overproduction and ATP de-synthesis, thus leading to oxidative damage and energy starvation. Finally, the intact microorganisms collapse and fragment, which causes membrane integrity destruction and intracellular matter leakage, eventually resulting in the loss of microbial viability, as illustrated in Scheme 1b. To further elucidate it, the energy band diagrams in Scheme 2 have

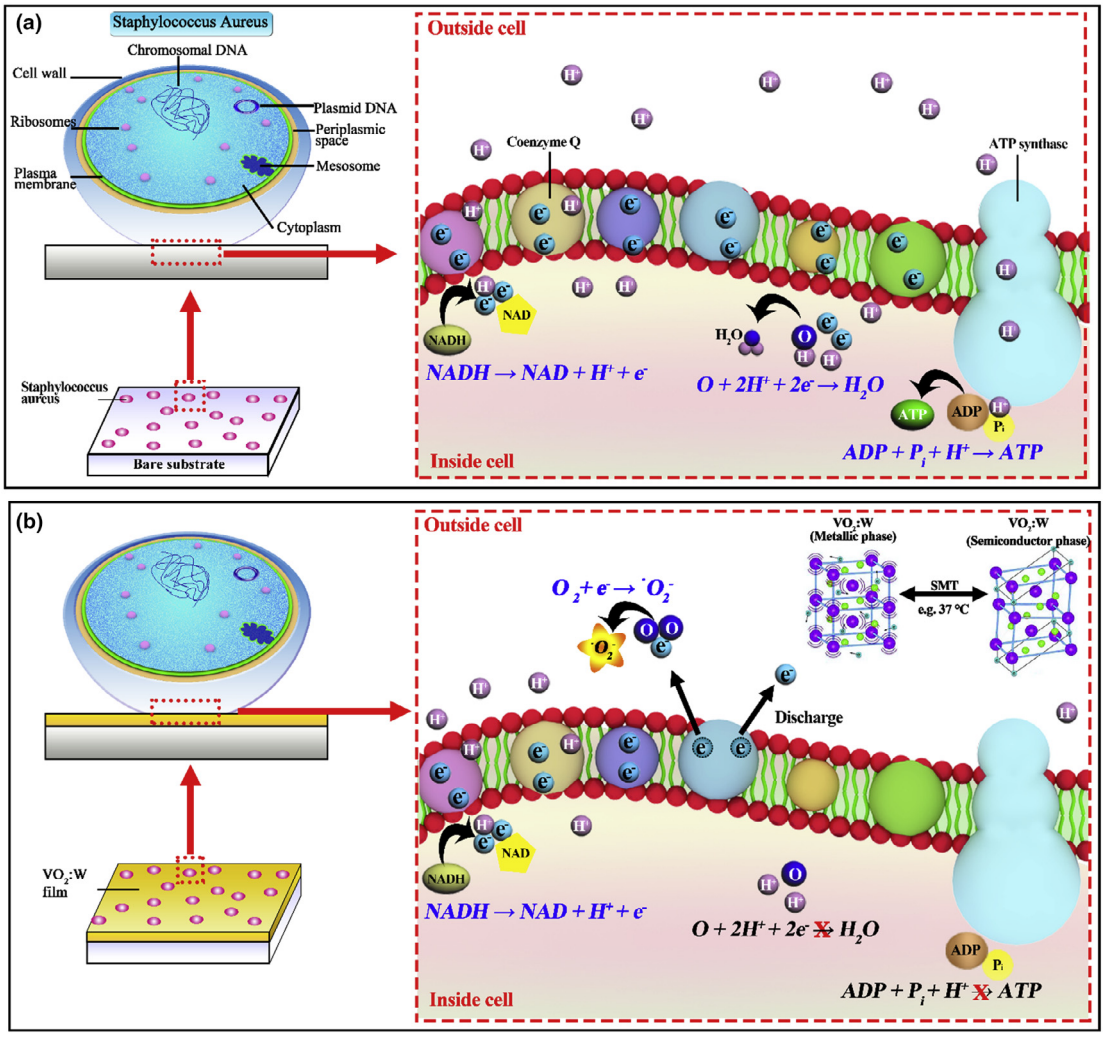

SCHEME 1

Schematic illustration elucidating the mechanism of electrically conductive VO_2 thin film acting as antifouling coating on a substrate to thwart biofilm formation: (a) When microorganisms initially adhere onto a bare substrate e.g., titanium or stainless steel, they can normally carry out extracellular electron transfer to terminal acceptor oxygen and ATP synthesis through respiration. (b) When microorganisms initially adhere onto VO_2:W film that can respond to environmental temperature e.g., body temperature 37 °C and transform from semiconductor phase to metallic phase, the direct physical contact induces the destructive electron extraction from transmembrane protein complex, a discharge process of respiratory chain, which thus causes ROS overproduction and ATP dyssynthesis, thereby leading to the oxidative damage and energy starvation and eventual electrocution of microorganisms.

been drawn in order to highlight the interactions between pure/W-doped VO_2 and the respiration chain in bacterial membrane. The biological redox potential (BRP) values of transmembrane protein complex in respiration chain are listed in Table S3. Based on the conversion equation of standard hydrogen electrode (E_0, V) and absolute potential level (E, eV) [54], $E_0 = -4.44 - E$, the BRP therefore ranges from −4.12 eV to −4.84 eV. Table S5 suggests the estimated energy levels of un-doped and doped VO_2 thin films at human body temperature (37 °C). Referring to our findings, Scheme 2a demonstrates the energy band diagram of VO_2 thin films and respiration chain, indicating that the VO_2 film in semiconducting phase can rarely extract electrons from the respiration chain, and then interrupt electron transfer process due to the conduction band in the range of BRP. In contrast, the W-doped VO_2 thin films can spontaneously extract electrons from the respiration chain and disrupt the BRP because of the Fermi level lower than BRP (Scheme 2b), thereby leading to the interruption of electron transfer process.

As a result, by W doping, the electrical conductivity of VO_2 films can be further enhanced to possess powerful electron trapping capability, which contributes to the observed antifouling activity to prevent biofilm formation. In fact, altering the electrical conductivity of the underlying substrate can also significantly influence the microbial behavior on the surface [55]. In fact, VO_2 is well known for its ultrafast reversible first-order semiconductor-to-metal transition at the critical temperature of ~68 °C, which serves as an active response to environmental temperature stimuli or near-infrared light irradiation (NIR) from infrared-transparent semiconductor phase (M1) to infrared-reflective metallic phase (R) [24,56]. This distinctive temperature-dependent phase change constitutes VO_2 to be a promising candidate of temperature-responsive or NIR-

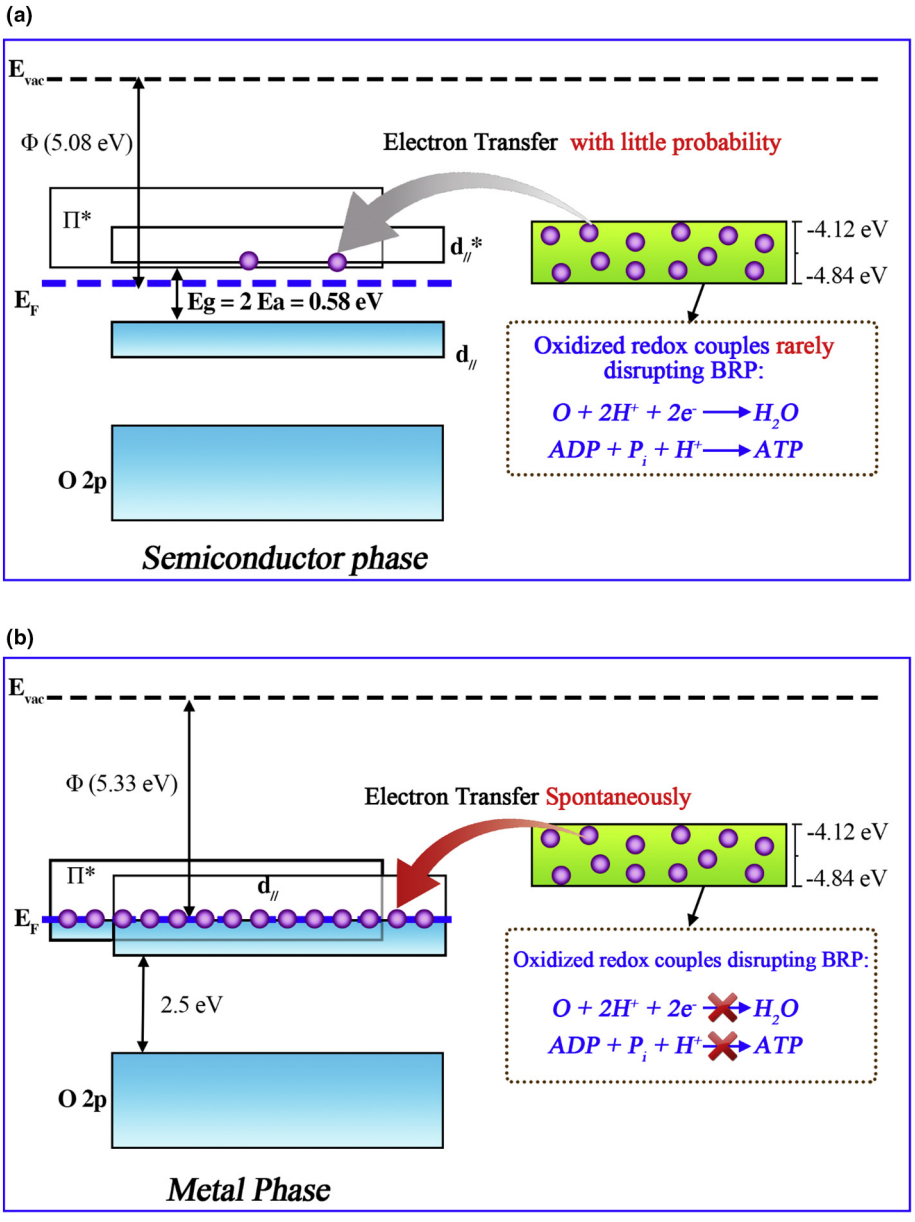

SCHEME 2

Schematic illustration of the energy band diagrams of VO_2 (a) and *VO–W3* (b) at human body temperature (37 °C) while interacting with the respiratory chain in bacterial membrane with BRP. (a) the semiconductor phase of VO_2 thin film can rarely disrupt BRP and electron transfer, whereas (b) the metal phase of *VO–W3* film can spontaneously disrupt BRP and electron transfer, thereby leading to electron leakage.

responsive intelligent material. As evidenced by this study, W doping can effectively modulate the VO_2 phase change initiated by temperature alteration and the thermochromic optical property just comes concomitantly. While exposing W-doped VO_2 to human body temperature (i.e., 37 °C) from room temperature, the semiconductor-to-metal phase change will be induced and lead to the concomitant dramatic change in electrical conductivity or band structure. Indeed, the change of electrical conductivity or band structure serves as the key factor of antifouling function. As a result, W doping can manipulate the phase change behaviors of VO_2 thin films. When the phase change of VO_2 film occurs at desired temperature, the electrical conductivity will be largely upregulated. For instance, when phase change of the film occurs at human body temperature and in contact with microorganisms, metallic VO_2 can perturb the normal physiological function of transmembrane proteins and consequently interrupt the electron transport along the respiratory chain. This will impede energy metabolism, cause oxidative damage and membrane leakage, electrocute microorganisms, and prevent biofilm formation. Most importantly, due to the advantage of using phase-change VO_2, the stimuli-responsive (temperature-responsive or NIR-responsive) antifouling function at a desired temperature can be achieved using W doping. As a result, the mechanism of increasing loss of MRSA viability on W-doped VO_2 films of metallic state is caused by the metallic, electrically conductive, VO_2-mediated electron leakage out of the microbial plasma membrane. In addition, the specific nano-patterns appearing on the thin-film surfaces may also contribute to the

antimicrobial effect. For instance, nickel nanostructures are able to alter the adhesion behaviors of *Staphylococcus aureus* on material surface [57]. Puckett et al. [58] also investigated the effects of nanorough, nanotubular and nanotextured titanium surfaces against the adhesion of *Staphylococcus aureus*. It was found that the bacteria unlikely adhered onto the nanorough surfaces, whereas the nanotubular surfaces provided a good environment for bacterial adhesion.

Conclusions

In summary, we have demonstrated the capability of W-doped VO_2 thin films to act as functional antifouling coatings. Microbial biofilms are ubiquitous on the surfaces of domestic, industrial, medical, and marine infrastructures/devices, and conventional biocides are increasingly problematic due to poor efficacy, nontarget environmental impact, and the evolution of resistance by microorganisms. Here, we show that W-doped VO_2 thin films with tunable phase change can exert temperature-responsive antifouling activity. When in contact with microorganisms, the electrically conductive VO_2 can disrupt membrane function and prevent biofilm formation. Targeting microbial membrane function is a promising strategy for impeding biofilm formation [59]. The deposition method is suitable for batch production for metal, glass, ceramic, or polymer substrates of various shapes, and the VO_2 films can even be deposited in arbitrary microscale patterns by masking specific areas to enable spatially patterned antifouling coatings. It is believed that these VO_2 systems can serve as an alternative strategy to overcome the current limitations of biofouling control.

Acknowledgments

This work was financially supported by National Natural Science Foundation of China (31370957, 81472109), Hong Kong Research Grant Council General Research Funds (CityU 11301215, CityU 11205617, HKU 718913, N_HKU726-16), City University of Hong Kong Donation Research Grant (9220061), Shenzhen Science and Technology Funding (JCYJ20160429190821781, JCYJ20160429185449249) and Guangdong Scientific Plan (2014A030313743).

Appendix A. Supplementary data

Supplementary data associated with this article can be found, in the online version, at https://doi.org/10.1016/j.mattod.2018.04.005.

References

[1] C.M. Magin, S.P. Cooper, A.B. Brennan, Mater. Today 13 (2010) 36–44.
[2] H.-C. Flemming et al., Nat. Rev. Microbiol. 14 (2016) 563–575.
[3] J.W. Costerton et al., Annu. Rev. Microbiol. 49 (1995) 711–745.
[4] J.W. Costerton, P.S. Stewart, E.P. Greenberg, Science 284 (1999) 1318–1322.
[5] L. Hall-Stoodley, J.W. Costerton, P. Stoodley, Nat. Rev. Microbiol. 2 (2004) 95–108.
[6] S.L. Chua et al., Nat. Commun. 7 (2016) 10750.
[7] S.R. Shah et al., Mater. Today 16 (2013) 177–182.
[8] D. Davies, Nat. Rev. Drug Discovery 2 (2003) 114–122.
[9] P.S. Stewart, J. William Costerton, Lancet 358 (2001) 135–138.
[10] D.I. Andersson, D. Hughes, Nat. Rev. Microbiol. 8 (2010) 260–271.
[11] S.B. Levy, B. Marshall, Nat. Med. 10 (2004) S122–S129.
[12] E.P. Ivanova et al., Nat. Commun. 4 (2013) 2838.
[13] M.S. Mannoor et al., Nat. Commun. 3 (2012) 763.
[14] S.Y. Reece, D.G. Nocera, Annu. Rev. Biochem. 78 (2009) 673–699.
[15] N.S. Malvankar et al., Nat. Nanotechnol. 9 (2014) 1012–1017.
[16] T.A. Clarke et al., Proc. Natl. Acad. Sci. U. S. A. 108 (2011) 9384–9389.
[17] R.S. Hartshorne et al., Proc. Natl. Acad. Sci. U. S. A. 106 (2009) 22169–22174.
[18] H.W. Harris et al., Proc. Natl. Acad. Sci. U. S. A. 107 (2010) 326–331.
[19] G. Reguera et al., Nature 435 (2005) 1098–1101.
[20] C.R. Myers, K.H. Nealson, Science 240 (1988) 1319.
[21] E.U. Donev et al., Phys. Rev. B 73 (2006) 201401.
[22] P. Markov et al., ACS Photonics 2 (2015) 1175–1182.
[23] J.Y. Suh et al., J. Opt. A: Pure Appl. Opt. 10 (2008) 055202.
[24] J.Y. Suh et al., J. Appl. Phys. 96 (2004) 1209–1213.
[25] D.W. Ferrara et al., Nano Lett. 13 (2013) 4169–4175.
[26] L. Whittaker, C.J. Patridge, S. Banerjee, J. Phys. Chem. Lett. 2 (2011) 745–758.
[27] Y. Gao et al., Nano Energy 1 (2012) 221–246.
[28] H. Zhou et al., Ceram. Int. 42 (2016) 7655–7663.
[29] J. Ye et al., J. Alloy. Compd. 504 (2010) 503–507.
[30] G. Silversmit et al., J. Electron Spectrosc. Relat. Phenom. 135 (2004) 167–175.
[31] W. Burkhardt et al., Thin Solid Films 345 (1999) 229–235.
[32] L. Su, H. Wang, Z. Lu, Mater. Chem. Phys. 56 (1998) 266–270.
[33] J. Shi et al., Sol. Energy Mater. Sol. Cells 91 (2007) 1856–1862.
[34] C. Tang et al., Phys. Rev. B 31 (1985) 1000–1011.
[35] Z.P. Wu et al., J. Appl. Phys. 86 (1999) 5311–5313.
[36] C. Ko, Z. Yang, S. Ramanathan, ACS Appl. Mater. Interfaces 3 (2011) 3396–3401.
[37] K. Martens et al., J. Appl. Phys. 112 (2012) 124501.
[38] A. Sohn et al., Appl. Phys. Lett. 101 (2012) 191605.
[39] Y. Zhou, S. Ramanathan, J. Appl. Phys. 113 (2013) 213703.
[40] A. Sohn et al., Sci. Rep. 5 (2015) 10417.
[41] N.B. Aetukuri et al., Nat. Phys. 9 (2013) 661–666.
[42] T.D. Manning et al., Chem. Mater. 16 (2004) 744–749.
[43] A. Romanyuk et al., Sol. Energy Mater. Sol. Cells 91 (2007) 1831–1835.
[44] L.D. Talley et al., Descriptive Physical Oceanography: An Introduction, sixth ed., Elsevier, 2011.
[45] R.J. French, P.J.H. Jones, Life Sci. 52 (1993) 339–346.
[46] J.L. Domingo, Reprod. Toxicol. 10 (1996) 175–182.
[47] N. Dennis Chasteen, The biochemistry of vanadium, in: M.J. Clarke et al. (Eds.), Copper, Molybdenum, and Vanadium in Biological Systems, Springer, Berlin Heidelberg, 1983, pp. 105–138.
[48] J.D. Jarrell, B. Dolly, J.R. Morgan, J. Biomed. Mater. Res. Part A 90A (2009) 272–281.
[49] A.E. Nel et al., Nat. Mater. 8 (2009) 543–557.
[50] A. Nel et al., Science 311 (2006) 622–627.
[51] F.Q. Schafer, G.R. Buettner, Free Radical Biol. Med. 30 (2001) 1191–1212.
[52] F. Natalio et al., Nat. Nanotechnol. 7 (2012) 530–535.
[53] P. Mitchell, Biochim. Biophys. Acta - Bioenerg. 1807 (2011) 1507–1538.
[54] X. Zhang, Y.L. Chen, R.-S. Liu, D.P. Tsai, Rep. Prog. Phys. 76 (2013) 046401.
[55] J. Li et al., Sci. Rep. 4 (2014) 4359.
[56] F.B. Nathaniel et al., J. Phys.: Condens. Matter 28 (2016) 125603.
[57] Z. Jahed et al., Biomaterials 35 (2014) 4249–4254.
[58] S.D. Puckett et al., Biomaterials 31 (2010) 706–713.
[59] J.G. Hurdle et al., Nat. Rev. Microbiol. 9 (2011) 62–75.